# High-performance triboelectric nanogenerators incorporating chlorinated zeolitic imidazolate frameworks with topologically tunable dielectric and surface adhesion properties

Jiahao Ye , Jin-Chong Tan [*]

*Multifunctional Materials & Composites (MMC) Laboratory, Department of Engineering Science, University of Oxford, Parks Road, Oxford OX1 3PJ, United Kingdom*

ABSTRACT

Triboelectric nanogenerator (TENG), a device that can convert mechanical energy into electricity based on the principle of triboelectrification, has gained tremendous attention since its first discovery in 2012. Although TENG has versatile applications in energy harvesting and self-powered sensing, its commercialization is still limited by the low power output. Recently, metal-organic frameworks (MOFs), with their large surface area and excellent tunability, have been explored to enhance the electrical performance of TENG. Herein, we synthesized nanoparticles of hydrophobic zeolitic imidazolate framework ZIF-71 (RHO topology) and its non-porous counterpart ZIF-72 (LCS topology), which were subsequently incorporated in a polydimethylsiloxane (PDMS) matrix as filler materials. By modifying the topology of ZIF nanofillers, we found the dielectric constant and surface adhesion of composites are both enhanced, thereby generating significantly higher triboelectric output. Moreover, we show the resultant ZIF/PDMS nanocomposite films exhibit enhanced triboelectric properties and long-term stability under cyclic mechanical loading. After integrating the prepared nanocomposite films into TENG devices, we accomplished the peak output voltage and current of 578 V and 19 µA for thin films ($3 \times 3$ cm$^2$, thickness ~0.33 mm), respectively, by embedding 1 wt % of ZIF-72 nanoparticles into PDMS matrix, with an instantaneous maximum power density of ~5 W m$^{-2}$. In this study, the mechanism of improved TENG performance by incorporating MOF nanoparticles has, for the first time, been revealed through nanoscale-resolved mechanical and chemical studies. Furthermore, the practicality of MOF-based TENG was demonstrated by harvesting energy from oscillatory motions, for powering up commercial microelectronics, transmitting electrical signals remotely, and functioning as a self-powered Morse code generator.

## 1. Introduction

Triboelectric nanogenerator (TENG) is an evolving technology first proposed by the Wang group in 2012 [1]. As a simple and cost-effective energy generating device, TENG is capable of transforming mechanical motions into electric energy, which can be harvested for a variety of scenarios, including self-powered sensors [2–5] and energy harvesters [6,7]. These applications have essential roles in the development of emergent technologies such as the Internet of Things (IoT) [8], wearable electronics [9], and artificial intelligence (AI) [10]. Although the concept of TENG was first introduced in the 21st century, the triboelectric effect, a fundamental physical phenomenon, has been observed for thousands of years, and a number of research have investigated the theory behind it [11–13]. Currently, the selection of materials for

triboelectric nanogenerators is commonly referred to the triboelectric series, ranked by the ability to attract or repel electrons through empirical results [14]. For the tribo-positive materials, metals like copper and aluminum are the conventional options attributed to their excellent electron-donating properties [15]. On the other hand, for tribo-negative materials, fluorinated polymers dominate the triboelectric series due to their high electronegativity and surface charge density [16]. Despite these materials having been present in the series for well over a decade, the practical applications of TENGs are still limited by the low power output. The challenge, therefore, is to develop new triboelectric materials beyond the ones present on the conventional triboelectric series with the aim for overcoming the current bottlenecks.

Through years of development, various strategies have been proposed to improve the electrical performance of TENG, including

---

material surface modification [16]. incorporation of filler materials as charge traps [17], and amplification of material's dielectric constant [18]. Among all approaches, the addition of nanoparticles as a filler material into conventional triboelectric materials is considered as the most convenient and effective to improve the triboelectric properties of a material from all above aspects. A variety of materials have been studied to improve the operating performance and the robustness of TENG, such as perovskites [19], MXenes [20], graphenes [21], carbon nanotubes [22], etc. Recently, metal-organic framework (MOF) material has gained tremendous attention due to its organic-inorganic hybrid structure. MOF is a class of material fabricated by the self-assembly of metal ions and organic linkers with formation of well-structured nanopores and high surface areas. The high flexibility and tunability of MOF enable functionalization of its structure for different applications such as sensing [23], luminescence [24], catalysis [25], and gas adsorption [26]. Likewise, these excellent properties can be leveraged for improving the output performance of TENG by tuning the dielectric constants [27,28], improving the surface charge density or controlling the surface roughness. In 2019, Wen et al. first developed a humidity resistive TENG by incorporating HKUST-1 within the PDMS polymer matrix [29]. Due to the remarkable electron trapping capacity and high dielectric constant of HKUST-1, the power output of prepared TENG increased by 13 times compared to that of TENG without MOF. Moreover, Jayababu and Kim fabricated a bimetal organic framework (BMOF) containing both cobalt and zinc metal ions which showed an enhanced TENG power output [30]. Ascribed to the tunable sensing properties of MOF materials, the fabricated TENG was tested to be employed as an ammonia sensor with great selectivity and durability. Besides, Rana et al. carbonized ZIF-67 to form a cobalt-containing nanoporous carbon (Co-NPC) and used it as a filler material for the charge generating layer of a non-contact mode TENG [31]. A filler loading of 3 wt % in the Ecoflex matrix improved the power output by 2 times due to the high porosity and charge trapping capacity of MOF. Later in 2021, Wen et al. further reported the approach of using ZIF-8 as a filler in PDMS matrix [32]. The addition of ZIF-8 nanoparticles was reported to increase the TENG output up to 176 V and 16.3 µA, over 2 times higher than that without ZIF-8.

In this work, a chlorinated zeolitic imidazolate framework (a subclass of MOF), Zn(4,5-dichloroimidazole)$_2$, commonly known as ZIF-71 with a RHO topology, is selected as the nanofiller for TENG applications. ZIF-71 has advantages such as ease of synthesis, moderate particle size, high resistance to humidity, and good compatibility with polymer matrices. Based on these excellent properties, we further modulated the topology of Zn(4,5-dichloroimidazole)$_2$ to a non-porous form with an LCS topology, named ZIF-72. On the contrary, ZIF-72, due to its dense framework structure and unconventional synthesis condition, was rarely studied in literature, yet its unique properties such as higher dielectric constant (amongst MOF structures) and excellent environmental stability could be favorable for practical TENG applications. By incorporating an optimum quantity of the above-mentioned MOF nanoparticles into PDMS matrix, TENG devices with much enhanced electrical performance were fabricated. We herein report for the first time by taking the unique advantage of non-porous MOF materials for improved electrical performance of TENG. By comparing the output performance of TENG based on MOFs with the same composition but different topology, this work provides valuable insights into the judicious selection of MOF as triboelectric materials. Based on our findings, we propose that the high external surface area of MOF is more advantageous for TENG applications compared with its internal surface area, as a denser framework will improve the dielectric constant for a higher triboelectric output. The presence of chlorine atoms in the ligand of ZIF-71 and ZIF-72 induced high electronegativity, hence improving the charge generating capability of the prepared ZIF/PDMS composites. The high external surface of MOFs incorporated in polymer matrix created a larger effective contact area which behaves as charge traps to draw electrons deeper into the film, creating more opportunities for charge transfer.

The effects of physical properties such as porosity, dielectric constant, mechanical property, and surface adhesion on the output performance were revealed under various nano-microscopy techniques and analyzed to establish the general design criteria for the selection of MOF in TENG. As a result, the prepared TENG devices fabricated by ZIF-71/PDMS and ZIF-72/PDMS nanocomposites both showed improved electrical output performance compared with a neat polymer, with ZIF-72/PDMS TENG achieving a high open-circuit voltage and short-circuit current of 578 V and 19 µA, respectively, which are 2.8 times and 4.2 times higher than the pristine PDMS TENG. An instantaneous power density of 5 W m$^{-2}$ was achieved under an external load resistance of 20 MΩ. Additionally, a prototype for a pedometer that can transmit signals remotely via Bluetooth and a Morse code generator device were designed to demonstrate the future potential of using the ZIF-72/PDMS TENG as self-powered sensors.

## 2. Methods

### 2.1. Materials

All chemicals used in this work are commercially available. Zinc acetate (Zn(OAc)$_2$·2H$_2$O), 4,5-dichloroimidazole (dcIm), zinc oxide (ZnO), and methanol were purchased from Sigma-Aldrich. Sylgard 184 (polydimethylsiloxane (PDMS) elastomer and curing agent) was obtained from Dow Corning.

### 2.2. Synthesis of MOF nanoparticles

(1) ZIF-71 nanoparticles were synthesized through a solution mixing method [33] performed under ambient conditions. 2.4 mmol of zinc acetate and 9.6 mmol of 4,5-dichloroimidazole were dissolved in 15 mL of methanol, respectively. After 1 h of homogenization, the two solutions were combined at ambient temperature and stirred for another 24 h to produce a white suspension product. The product was then centrifuged at 8000 rpm for 10 min and washed three times in methanol to remove excess ligands. After drying at room temperature overnight, the resulting ZIF-71 powder was obtained. (2) ZIF-72 nanoparticles were synthesized through a solvent-free, high-temperature method [34]. Initially, 2 mmol of zinc oxide powder was physically mixed with 6 mmol of 4,5-dichloroimidazole inside a 50 mL Schott bottle. Then the Schott bottle was capped and heated at 150 °C for 24 h. The as-synthesized powder product was then washed with excessive methanol to dissolve the unreacted ligands and then centrifuged at 10,000 rpm for 10 min. After three washing cycles, the yellowish ZIF-72 powder was dried overnight.

### 2.3. Preparation of ZIF/polymer nanocomposite

The ZIF/PDMS composite film was prepared by doctor blade casting. PDMS elastomer was first combined with the curing agent at a weight ratio of 10:1. The synthesized MOF particles (crystals of ZIF-71 and ZIF-72) were then added to the PDMS solution at different weight ratios of 0, 1, 2, 3, 4 and 5 wt %, respectively. After being dispersed homogeneously by a motor-driven blender overnight, the ZIF/polymer mixture was dripped on a glass substrate and casted by a doctor blade with a defined gap size to obtain a film with uniform thickness. The cast film was then cured at 100 °C for 30 min in a vacuum oven and peeled off from the substrate. The prepared ZIF/PDMS composites were cut into small pieces with a dimension of 3 cm × 3 cm for subsequent tests. The average thickness of the prepared nanocomposite films was determined to be ca. 330 ± 30 µm.

### 2.4. Fabrication of TENG devices

TENG devices were fabricated in the contact-separation mode. To

ensure a flat contact surface, a pair of 3D-printed boards with a contact area of 3 cm × 3 cm was used as the substrate for fabricating a TENG device. The customized board was designed to have a uniform force distribution during oscillatory contact and maintain a low energy loss through jumper wires. A piece of aluminum (Al) foil was used as the negative electrode adhered to one of the boards by a double-sided adhesive. The prepared ZIF/PDMS nanocomposite film was then attached to the Al foil to form the tribo-negative layer. Another piece of Al foil was pasted on the other board to act as both the tribo-positive layer and the counter electrode. Three types of TENG devices were prepared by neat PDMS (P-TENG), ZIF-71/PDMS (Z71-TENG), and ZIF-72 PDMS (Z72-TENG). The periodic contact-separation movement of TENG was driven by a permanent magnet shaker (Brüel & Kjær LDS V201) powered by a voltage-amplified arbitrary function generator (GW Instek AFG-2105). In a standardized test, the operating parameters comprising frequency (2 Hz), maximum impact force (16 N), and amplitude of displacement (4 mm) for the magnetic shaker were applied. The optimum separation gap of 4 mm was selected to be a standard based on experimental results as it achieved the highest electrical output by balancing the effect of impact force and electrostatic potential between the TENG electrodes.

### 2.5. Materials characterization

The surface morphologies of the as-prepared MOF materials were characterized by a field-emission scanning electron microscope (FESEM LYRA₃ GM TESCAN). The crystalline structures of MOF and nanocomposites were analyzed by X-ray diffraction (XRD) using a Rigaku MiniFlex with a Cu Kα source (1.541 Å). The Brunauer-Emmett-Teller (BET) surface area of MOF was determined by the N2 physisorption measurements at 77 K (Autosorb iQ Station 2). The atomic force microscope (AFM) height topography and nano-FTIR spectra (at ~20 nm resolution [35]) of the nanoparticles and nanocomposites were determined from a scattering-type scanning nearfield optical microscope (Neaspec s-SNOM). A Nicolet iS10 FTIR spectrometer equipped with an attenuated total reflectance (ATR) module was used to record the Fourier-transform infrared (FTIR) spectrum. The far-IR spectroscopy was performed at the multimode IR imaging and microspectroscopy (MIRIAM) Beamline B22 at the Diamond Light Source synchrotron via a Bruker Vertex 80v FTIR spectrometer, equipped with an ATR accessory (Bruker Optics). The dielectric measurements were assessed by an LCR meter (Hioki IM3536) as a function of frequency sweeping from 4 Hz to 8 MHz. The output voltage was measured by an oscilloscope (Rigol DS1054Z) with a 100 MΩ high voltage probe (Rigol RP1300H). The output current and charge transfer of the device were measured by an electrometer (Keithley 6514) and a multifunctional impedance spectrometer (IviumStat.h).

### 2.6. Numerical modeling

The variation of electric potential was simulated using the finite element method (FEM) implemented in the COMSOL Multiphysics software. The simulation was performed by the electrostatics analysis model. The geometry of the simulated triboelectric nanogenerator device was created to match the dimensions of the actual experiment (an area of 3 cm × 3 cm for electrodes and composite material, with a maximum separation gap of 4 mm between the electrodes). Aluminum was selected as the material for the top and bottom electrodes, and the material properties of the ZIF/PDMS composite films were specified based on experimental measurements. The boundary conditions for the simulation were defined by employing the dielectric surface charge density measured on the composite surface and the electrode potential under open-circuit condition. Stationary studies were then performed with respect to the variation of displacement between the electrodes to predict the resultant electrical potentials across the triboelectric nanogenerator device.

## 3. Results and discussion

### 3.1. Composite films of ZIF/PDMS

ZIF-71 and ZIF-72 nanoparticles were constructed through the self-assembly of the $Zn^{2+}$ cations and dcIm linkers, as illustrated in Fig. 1a. However, the variation of reaction conditions resulted in two distinctive framework topologies and physico-chemical properties. The SEM micrographs of the single nanoparticles of ZIF-71 and ZIF-72 are shown in Fig. 1b and c. Dissimilar crystal morphologies have been observed for ZIF-71 and ZIF-72. Specifically, ZIF-71 is a rhombic dodecahedron nanocrystal with well-defined facets, whereas ZIF-72 nanoparticles exhibit no specific morphology. Based on the AFM height topography shown in Fig. 1d-g, the lateral crystal size of ZIF-71 was found to be ~730 ± 130 nm with a height of ~250 ± 60 nm. In contrast, ZIF-72 has a relatively smaller particle size of ~150 ± 60 nm, and with a stronger tendency to form aggregates.

The FTIR spectra of prepared nanoparticles in both mid-IR and far-IR regions are shown in Fig. 2a and b, respectively. Due to the same constituting dcIm ligand and corresponding functional groups, ZIF-71 and ZIF-72 show similar vibrational modes. However, some minor differences are identifiable due to the difference in their coordination structure. The shifts of peaks are observed at 1466 cm$^{-1}$ for N − CH bending, and 1202 cm$^{-1}$ for CH bending. Some distinct peaks also exist for ZIF-72 at 1414 cm$^{-1}$ and 1350 cm$^{-1}$ which originate from the different topological arrangement of atoms within the framework structure. Within the far-IR region, similar results are identified with subtle differences detected in the terahertz (THz) collective modes due to the metal-ligand interactions. Moreover, by incorporating the ZIF-71 and ZIF-72 fillers into the PDMS matrix, there is no obvious band shifting observed from the FTIR spectra, which imply minimal chemical interactions between the fillers and the PDMS matrix, and thus no sign of decomposition of the MOF fillers. The superimposed FTIR result shows a clearer view of the relationship between the peak height at 1202 cm$^{-1}$ and the amount of MOF loading (wt %), as shown in Fig. S1 of the Supplemental information (SI).

Fig. 2c shows the crystallinity of the as-synthesized ZIF-71 and ZIF-72 nanoparticles, characterized by powder XRD. Both diffraction patterns are consistent with the simulated pattern, indicating the successful fabrication of the MOF structures. It can be seen that ZIF-71 with an RHO topology shows Bragg peaks at 2θ angles of 4.4° and 7.6°, whereas ZIF-72 with an LCS topology exhibits salient peaks at 12.7° and 16.9°. Meanwhile, after the incorporation of MOF nanoparticles into PDMS matrix, the intensity of the main Bragg peaks increases with higher MOF loading which suggests a homogeneous dispersion of nanoparticles within the polymer matrix, and the crystallinity of ZIFs was retained, as shown in Fig. S2. The surface morphologies of the composite films of ZIF-71/PDMS and ZIF-72/PDMS are shown in Figs. S3 and S4.

### 3.2. Contact electrification and the effect of dielectric constant

Fig. 2d illustrates the structure of a conductor-to-dielectric contact-separation mode TENG, prepared using the ZIF/PDMS nanocomposites. The as-prepared composite film with a size of 3 cm × 3 cm was sandwiched between a pair of Al electrodes, the former acts as a tribo-negative layer for charge generation and charge storage. The working principle of a contact-separation mode TENG can be explained using the proposed electron transfer model [2,36]. At the initial stage (Fig. 2d(i)), the top electrode is not contacted with ZIF/PDMS nanocomposite film, and no charge transfer occurs between the electrodes. When the top electrode and ZIF/PDMS nanocomposite come into contact under the application of an external force (Fig. 2d(ii)), equal and opposite charges are induced on the contacting triboelectric surfaces due to tribo-electrification. The high electron affinity of the ZIF/PDMS nanocomposite attracts the electrons from the more electron-donating Al metal layer on its top. As a result, the nanocomposite layer becomes
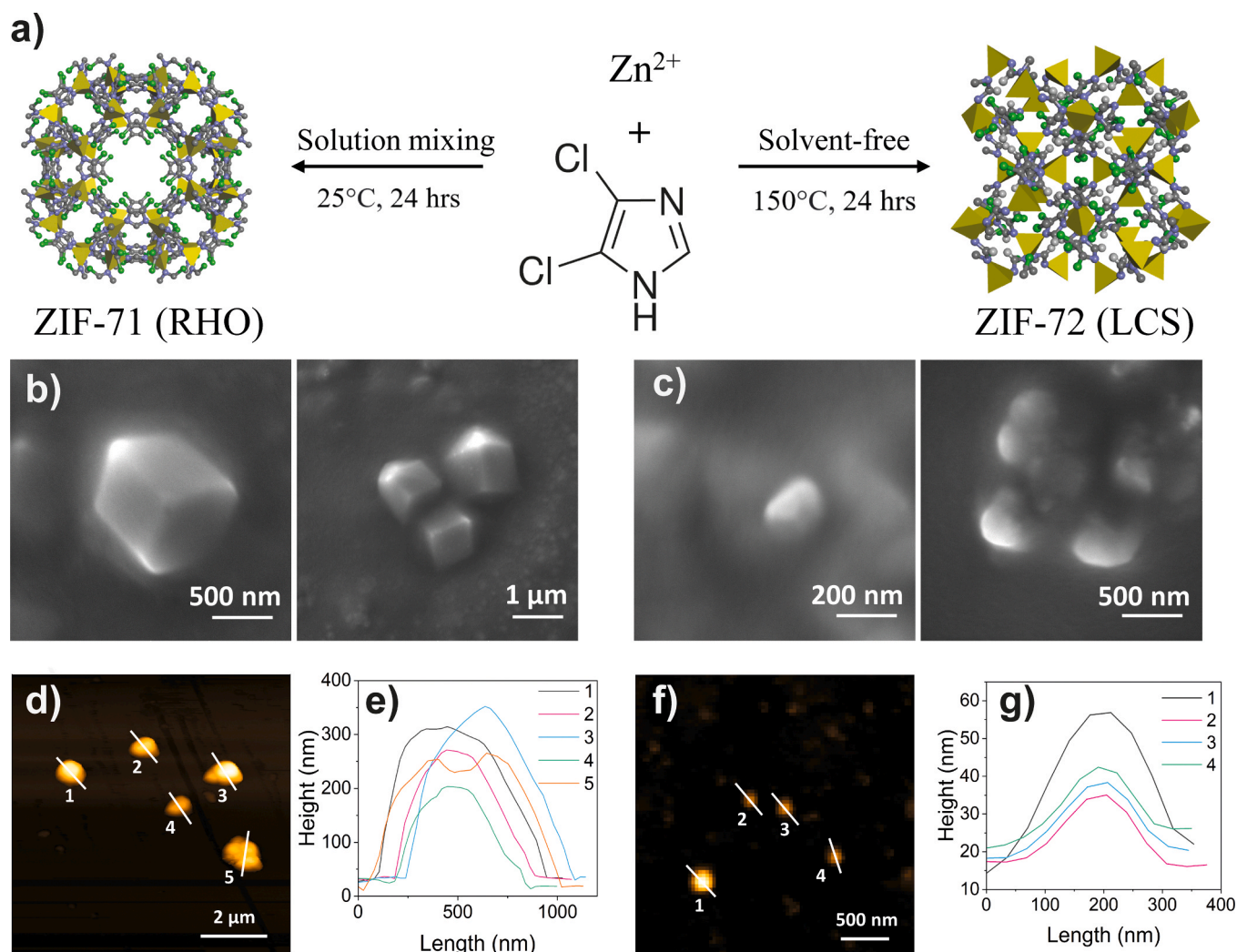
**Fig. 1.** (a) Schematics illustrating the synthesis routes of ZIF-71 (RHO topology) and ZIF-72 (LCS topology) nanoparticles (color scheme: ZnN$_4$ tetrahedron in yellow, nitrogen in purple, carbon in gray, hydrogen in white, and chlorine in green). (b) SEM micrographs of ZIF-71 nanocrystals. (c) SEM micrographs of ZIF-72 nanocrystals. (d,e) AFM height topography of ZIF-71 single crystals and the corresponding cross-sectional profiles. (f,g) AFM height topography of ZIF-72 single crystals and the corresponding cross-sectional profiles.

negatively charged, while the top metal electrode acquires a positive charge of equal magnitude. Subsequently, when the contacting force is released (Fig. 2d(iii)), the nanocomposite layer separates from the top electrode and a potential difference is induced, driving the electrons to flow from the bottom electrode to the top electrode through the external circuit. When the contact force is completely released and a fully separated state is reached (Fig. 2d(iv)), the electrons stop flowing. Subsequently, when the top metal electrode is brought into contact again (Fig. 2d(v)), it approaches the highly electronegative nanocomposite layer, causing the electrons to flow in the reverse direction. The flow of electrons stops when a fully contacted state is reached again (Fig. 2d(ii)). Through periodic contact and separation cycles, an alternating current (AC) output can be generated. For a conductor-to-dielectric contact-separation mode TENG, the potential difference between the triboelectric materials ($\Delta V$) can be expressed as [37],

$$\Delta V = E_d d + E_{air} x(t) = -\frac{Q}{S\varepsilon_0}(d_0 + x(t)) + \frac{\sigma x(t)}{\varepsilon_0} \tag{1}$$

where $E_d$ is the electrical field strength of dielectric material (in this case, the ZIF/PDMS nanocomposite), $d$ is the thickness of the dielectric material, $x(t)$ is the distance between the plates as a function of time, and $Q$ is the electrical charge transferred between the two electrodes. $\varepsilon_0$

and $\varepsilon_d$ are the permittivity of vacuum and the relative permittivity of the dielectric material, respectively. $d_0$ represents the effective thickness constant ($d_0 = d/\varepsilon_d$), and $\sigma$ is the surface charge density. Under open-circuit condition, where no electric charge is transferred between the two electrodes ($Q = 0$), the open-circuit voltage ($V_{oc}$) of TENG can be simplified as,

$$V_{oc} = \frac{\sigma x(t)}{\varepsilon_0} \tag{2}$$

From Eq. (2), it can be seen that the surface charge density of the dielectric material is a crucial parameter to determine the output voltage, and can be further expanded to [38],

$$\sigma = \frac{\varepsilon_0 \varepsilon_d V_{tri}}{d} \tag{3}$$

where $V_{tri}$ is the triboelectric voltage that is dependent on the material itself. According to Eq. (3), the dielectric constant of material ($\varepsilon_d$) corresponds to one of the most important properties for TENG output. By modulating the topology of ZIF-71 to ZIF-72, the dielectric constant of the nanocrystal is improved from 3.0 to 4.5 at 1 MHz, as shown in Fig. 2e. The higher dielectric constant of ZIF-72 compared with ZIF-71 can be attributed to its non-porous structure. The porosity level was confirmed by N$_2$ adsorption–desorption isotherms at 77 K (Fig. S5),
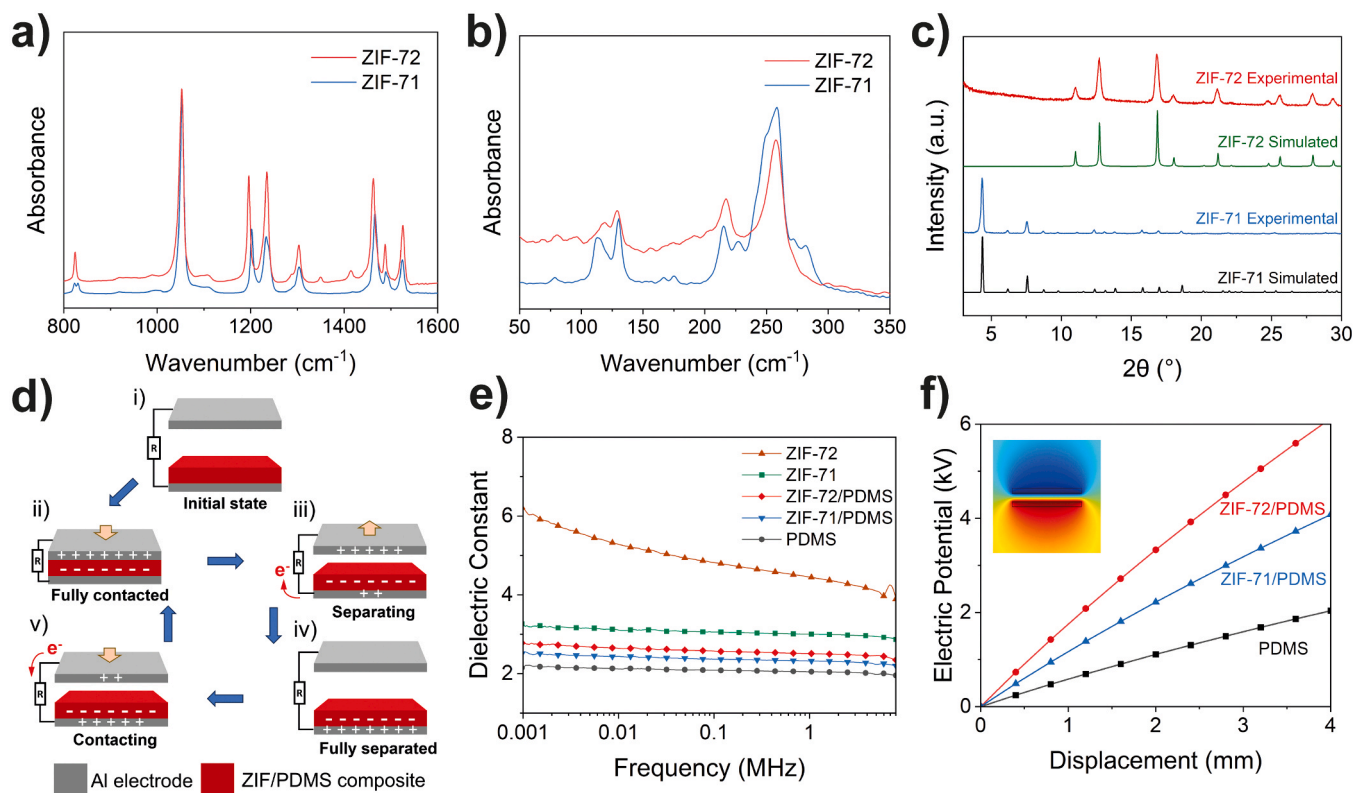
**Fig. 2.** FTIR spectra of the as-synthesized ZIF-71 (a) and ZIF-72 (b) nanoparticles in the mid-IR and far-IR regions, respectively. (c) XRD patterns of as-synthesized ZIF-71 and ZIF-72 nanoparticles compared with the simulated patterns (generated from crystallographic information file (CIF) in the Cambridge Structural Database (CCDC code: GITVIP and GIZJUV)). (d) Schematic diagram of the working mechanism (i-v) of a conductor-to-dielectric contact-separation mode TENG, based on ZIF/PDMS nanocomposite. (e) Dielectric constants of ZIF-72 pellet, ZIF-71 pellet, ZIF-72/PDMS (1 wt %), ZIF-71/PDMS (2 wt %), and pristine PDMS films, measured from 4 Hz to 8 MHz. (f) FEM predictions of electric potentials on the triboelectric material surfaces as a function of displacement between the pair of electrodes (as depicted in (d)).

where the BET surface areas of (porous) ZIF-71 and (dense) ZIF-72 were determined as 874 $m^2$/g and 5.6 $m^2$/g, respectively. Normally, a material with high volumetric density and highly polar molecular groups tends to have a higher dielectric constant [39]. Likewise, a porous MOF structure is known to exhibit a smaller value of dielectric constant due to the presence of air ($\varepsilon_d \sim 1$) in the pores [40,41]. Since ZIF-71 and ZIF-72 structures comprise the same dcIm linker with abundant and polar C−Cl bonds, the difference in their volumetric densities in consequence of their structural topology played a critical role to their dielectric constants. For ZIF-71, the existence of its nanopores hinders its polarizability and reduces the effective dielectric property. In contrast, the dense framework structure of ZIF-72 has a significantly lower porosity, thereby resulting in greater polarizability. The theoretical density of ZIF-72 determined from its crystal structure is 1.77 g $cm^{-3}$, whereas ZIF-71 has a relatively lower density of 1.15 g $cm^{-3}$. Therefore, the higher volumetric density of ZIF-72 leads to a larger dielectric constant. Fig. 2e also shows the measured dielectric properties of the pristine PDMS (neat), ZIF-71/PDMS and ZIF-72/PDMS thin films under a broad range of frequencies from 4 Hz to 8 MHz. With the incorporation of ZIF-71 nanoparticles into the neat PDMS ($\varepsilon_d \sim 2.05$), the dielectric constant was found to be improved, with the highest dielectric constant of 2.3 achieved at 2 wt % of ZIF-71 at a frequency of 1 MHz. On the other hand, incorporation of ZIF-72 further improved the dielectric constant up to 2.5 under a filler loading of 1 wt %. Both MOFs were found to improve the dielectric constants of the PDMS film with a similar trend. This increment of dielectric constant can be explained by the formation of micro-capacitors as MOF nanoparticles are incorporated into the polymer matrix. The nanoscale capacitor networks increase the polarizability of the MOF-based nanocomposite material, and as a result they enhance the dielectric properties. However, as the MOF loading

increases beyond a threshold value (see Fig. S6) a decline in dielectric constant was observed, this could be attributed to the adverse effect of filler aggregation.

An FEM simulation was also performed using the COMSOL software to model the electric potential generated between the two electrodes of a TENG device, as shown in Fig. 2f. Experimental measurements of dielectric constant (at 1 MHz) and surface charge for different materials were applied as inputs for the FE simulation. The general trend of electrical potential during operation is inline with the proposed working principle, which increases with a larger separation distance between the pair of electrodes. ZIF-72/PDMS composite with higher dielectric constant also shows a much higher electrical potential compared with ZIF-71/PDMS and neat PDMS polymer, indicating the important role of dielectric constant. We note the overpredictions in the magnitude of the output voltages, which can be ascribed to the idealized model and lossless boundary conditions imposed in the model, compared with real materials with imperfections as observed in the experiments.

### 3.3. Output performance of ZIF/PDMS TENGs

The output performance of the assembled MOF-TENG was measured on a customized test bench to study the effect of nanoparticle embedment. The open-circuit voltage, closed-circuit current, and charge transfer between the electrodes of TENG were measured for both Z71-TENGs and Z72-TENGs at different wt % loadings. Fig. S7 shows the experimental setup for the electrical output performance of TENGs and the dimensions of the fabricated nanocomposite films. Fig. 3a and b show the relationship between the filler loading in polymer matrix and the electrical performance of the device. For Z71-TENG, it was established that a 2 wt % composite exhibits the most outstanding electrical
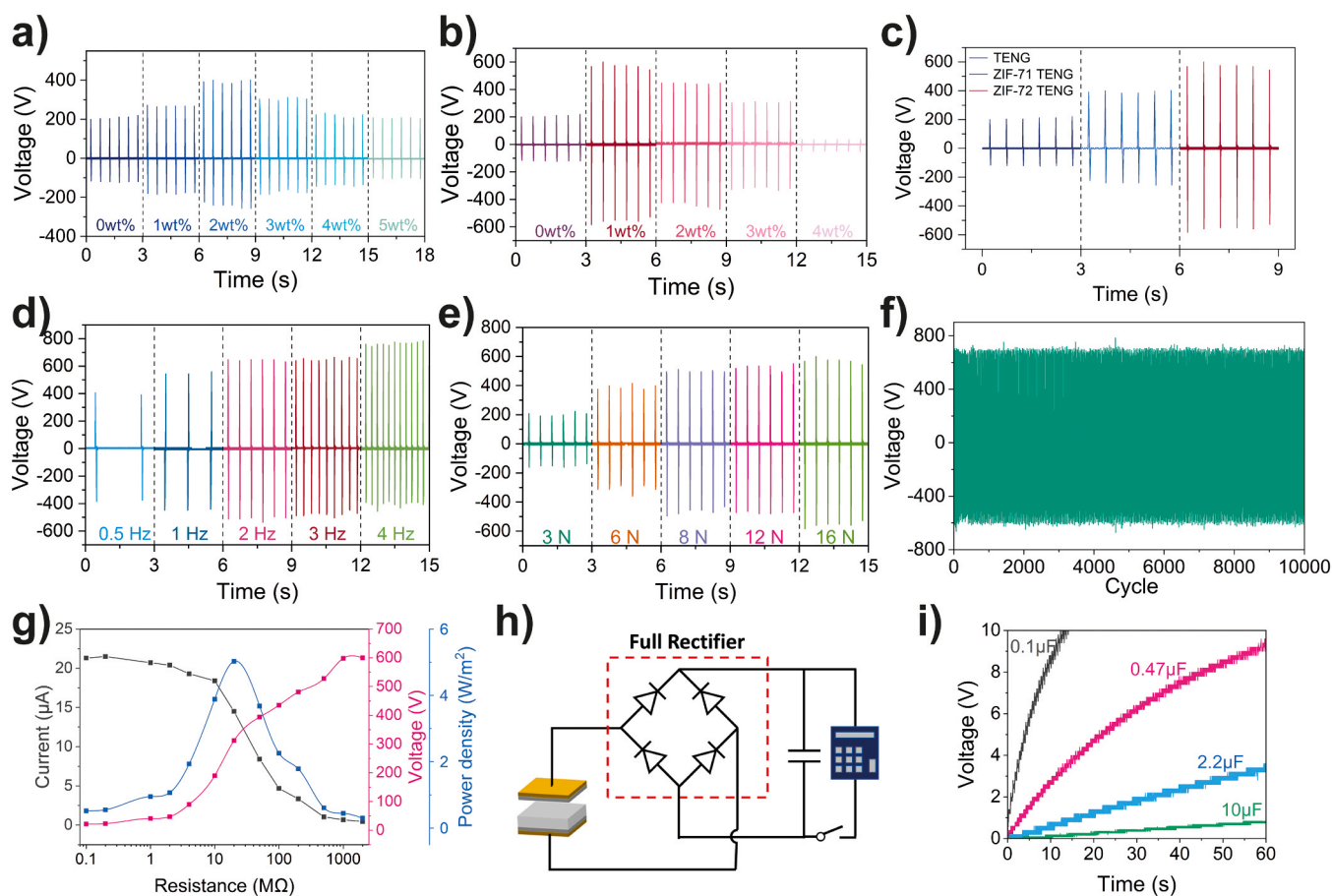
**Fig. 3.** (a) Open-circuit voltage of Z71-TENG at different mass loadings (wt %) under an oscillatory motion of 2 Hz. (b) Open-circuit voltage of Z72-TENG at different mass loadings under an oscillatory motion of 2 Hz. (c) Comparison of electrical output performance between Z72-TENG (1 wt %), Z71-TENG (2 wt %), and P-TENG under 2 Hz oscillatory motion with 16 N impact force. (d) Electrical output performance of Z72-TENG at 16 N under different frequencies. (e) Electrical output performance of Z72-TENG at 2 Hz with varying impact forces. (f) Durability test of the Z72-TENG subject to a continuous test of 10,000 impact cycles. (g) Peak voltage, current, and power density of Z72-TENG as a function of load resistance. (h) Schematic of an electrical circuit designed for the practical application studies of Z72-TENG. (i) Capacitor charging curves by operating Z72-TENG at 2 Hz for 0.1, 0.47, 2.2, and 10 μF capacitors.

performance with nearly doubled improvement of all electrical properties compared with the neat PDMS film, as shown in Fig. S8. Besides, the Z72-TENGs show a similar trend to Z71-TENGs, with the highest power output observed for the 1 wt % composite film. A remarkably high electrical output was obtained with an open-circuit voltage of 578 V, a peak-to-peak voltage of over 1139 V and a closed-circuit current of 19 μA, over 4 times higher than the neat PDMS film under identical test conditions. It is also worth noting that a reduction of output power was observed at higher MOF loadings. Such a decline can be attributed to the aggregation of nanoparticles at a higher mass concentration within the polymer matrix, which can also be observed in the SEM micrographs (see Fig. S3).

To have a closer look at the effect of embedding MOF nanoparticles into the matrix of a triboelectric composite material, the films of the highest electrical output were selected and compared with the pristine PDMS film, as shown in Figs. 3c and S10. The incorporation of MOFs shows a significant improvement in terms of the charge generating and charge trapping capacities of MOF nanoparticles. The presence of chlorine atoms in the ligand of ZIF-71 and ZIF-72 induces high electronegativity [42], hence improving the charge generating capability of the composite films. Moreover, more trapping sites are created by the uniform distribution of nanoparticles within the polymer matrix which can facilitate the charge transfer and charge storage within the composite. These trapping sites also hinder the charge recombination effect at the material surface during contact electrification, whereby drawing more charges to the inner structure of the material. On this basis, it can

be reasoned that more induced charges can be collected at the chlorinated groups of ZIF-71 and ZIF-72 nanofillers, thereby enhancing the overall charge density of the material.

In addition to the study on the effect of mass loading, the frequency dependency of the electrical performance was also investigated under a range of frequencies from 0.5 Hz to 4 Hz generated by the magnetic shaker. Results in Fig. 3d reveal that the output voltage of the Z72-TENG showed an increasing trend with rising input frequency of the impactor. With an increase in the operating frequency, an unsymmetric voltage profile was observed due to the varying strain rates of the magnetic shaker [43]. We hypothesize that the higher frequency results in a faster contact speed, leading to a higher positive voltage. Meanwhile, the insufficient displacement during separation causes a lower absolute value of the negative voltage.

Moreover, the influence of the applied force on the output performance was investigated under varying forces from 3 N to 16 N at a 2 Hz input frequency. The force of the impact was controlled by the voltage supplied to the magnetic shaker and measured by a calibrated force transducer. Fig. 3e and Fig. S12 show the correlations between the impact force and output voltage, current, and charge. Specifically for the output voltage, a linear correlation can be found at the lower-force region (0–10 N), where the TENG device exhibits a higher sensitivity of 63.4 V/N with good linearity. Therefore, there is scope for deploying the Z72-TENG as a self-powered force sensor, and it is worthwhile to investigate this avenue in future. The durability of the Z72-TENG device was also tested, since a long working time and stable power output is

crucial for practical implementations. To verify its robustness, the variation of its voltage output over continuous operation of 10,000 cycles under 2 Hz was recorded and shown in Fig. 3f. Moreover, the durability of prepared Z72-TENG and Z71-TENG over 50,000 cycles was tested under 5 Hz as shown in Fig. S14. At a longer run of 50,000 cycles, a relatively stable voltage was delivered throughout the cyclic tests, with an overall degradation of 10.6 % in peak voltage observed for Z72-TENG. During the cyclic impact, the prepared ZIF-72/PDMS nanocomposite showed good structural resilience and excellent attachment to the metal electrode. There was no significant change on the morphology of contacting surfaces, and structural integrity of electrode and nanocomposite was well-retained, as shown in Fig. S16.

The fabricated MOF-TENG devices were then connected into a closed circuit with varying load resistances, to examine the optimum operating conditions and to validate the practicability for real-world applications. Under a constant input frequency of 2 Hz and a compression load of 16 N, the closed-circuit voltage ($V_{sc}$) and closed-circuit current ($I_{sc}$) across the load resistor were measured, with power density $P_d$ calculated using the equation $P_d = (V_{sc}I_{sc})/A$, where $A$ is the nominal contact area. As shown in Fig. 3g, the Z72-TENG achieved a maximum power output of $5\ W\ m^{-2}$ employing a load resistance of 20 MΩ, with measured voltage and current showing an inverse relationship due to ohmic loss. Notably, the optimum operating resistance of Z72-TENG is lower than pure PDMS-based TENG reported in other studies [44] due to the improved capacitance from the addition of ZIF-72. This optimum resistance corresponds to the internal resistance of the generator, where a low impedance can lead to a broader application in real life [45]. Furthermore, the improvement achieved in voltage, current, and output power density by Z72-TENG is compared with other reported works of PDMS-based TENG, as summarized in Table S1. For instance, in comparison to the study conducted by Guo *et. al* [46], where a fluorinated MOF, KAUST-8 was incorporated in PDMS as triboelectric material, although a similar maximum voltage was achieved, our Z72-TENG exhibited an order of magnitude higher current output and power density. Previous studies have also explored other MOF@PDMS composite materials, including ZIF-8 [32], UiO-66 [47], and its derivatives [48], and our Z72-TENG demonstrates 3.3, 2.8 and 3.0 times higher peak voltage output compared with these studies respectively. Although the experimental setup in each study is different in frequency, force, and exact configuration, broadly it can be seen that the electrical performance of Z72-TENG prepared in this study are positioned among the highest-performing works in the field.

### 3.4. Charging and discharging of portable commercial electronics and LEDs

To verify the effectiveness of TENG as an energy harvester, the alternating current produced by TENG was harvested and stored into capacitors through a full rectifier circuit, shown in Fig. 3h. After induced charges passing through the rectifying circuit, the alternating current was converted to direct current by a network of diodes, therefore reducing the energy loss during the charging process. The rectified current can be subsequently used to charge up capacitors and other small consumer electronics. As shown in Fig. 3i, several commercial capacitors with capacitances ranging from 0.1 μF to 10 μF were charged by a steady 2 Hz oscillation motion and 16 N compression load. A reasonably high charging voltage can be attained for all capacitors after a relatively short time of ~1 min, with less charging time required for smaller capacitors. More specifically, the result shows a charge voltage of 10 V for a 0.1 μF capacitor within 15 s, which suggests the feasibility to redistribute the stored electricity to other electronics. The difference in the charging speed to a 2.2 μF capacitor by Z72-TENG, Z71-TENG, and P-TENG is compared in Fig. S17. The prepared Z72-TENG shows significantly higher energy harvesting rate under the same testing conditions. For verification, a 47 μF capacitor was first charged to 3 V by the Z72-TENG and subsequently used to power up microelectronics,

including a humidity thermometer, a digital timer, a calculator, and an array of LEDs. The charge-discharge curves for the different electronics are displayed in Fig. S18. Video S1 shows the charging of a commercial calculator. As the selected electronics have distinct operating voltage and power consumption rates, the operational time for each electronic was also recorded. We found that the charged capacitor can successfully power up all these electronics, with the calculator having the longest standby time among the four, where the number displayed on its screen remained visible after 30 s of operation. The illumination of 300 LEDs powered by the Z72-TENG was also demonstrated in Fig. S19 and Video S2.

Supplementary material related to this article can be found online at doi:10.1016/j.nanoen.2023.108687.

### 3.5. Probing triboelectrification mechanism of ZIF/PDMS composites via nanoanalytics

To further investigate the fundamental triboelectrification mechanism of ZIF/PDMS composites, we employed the near-field s-SNOM technique in combination with nano-FTIR and tip-force microscopy (TFM) technique to reveal the local chemical and mechanical information at a resolution of 20 nm. The nano-FTIR spectra of ZIF-71 and ZIF-72 single crystals shown in Fig. 4a-c are consistent with ATR-FTIR results (Fig. 2a), with the main characteristic peak at around 1050 cm$^{-1}$ corresponding to the in-plane deformation of the imidazole ring [49]. After incorporating ZIF-72 nanoparticles into PDMS matrix, this main peak of nanofillers remains detectable from nano-FTIR taken across the composite, as shown in Fig. 4d-e. Although the characteristic peaks for PDMS at 1100 cm$^{-1}$ and 1263 cm$^{-1}$ still dominate at sampling points 1 and 3 as ZIF-72 particles are partially buried beneath the cross-linking of PDMS matrix, these nanoparticles are close enough to the material surface to alter the properties of the interface. Consequently, we propose that this nanoscale compositional variation at the near surface layer will lead to formation of charge traps by dissimilar functional groups with enhanced electron affinity, thereby generating higher triboelectric output.

The nanoscale mechanical properties at the composite surfaces were further investigated by TFM. As shown in Fig. 4f-i, the ZIF-71 and ZIF-72 nanoparticles present at the surface significantly have improved the surface adhesion of PDMS matrix to an order of magnitude higher. Previous research has found close relationship between adhesion energy and triboelectric output [43,50]. The nanostructure of ZIF-72 with high adhesion energy on PDMS surface improves the stress of contact and separation. As a result, the higher stress facilitates the energy conversion towards triboelectric energy and improves the amount of surface charge transfer [51]. The effect of adhesion force on the triboelectric output can also be revealed through the output voltage profile of TENG devices. As shown in Fig. 3b, Z72-TENG shows higher output voltage during separation with a more negative peak value compare with P-TENG. This finding can be explained by the higher acceleration during material detachment due to the greater adhesion force of ZIF-72/PDMS. The high separation acceleration resulted in strong electrostatic potential, thus more charge can be transferred. In addition, from the AFM height topography images shown in Fig. S20, the surface roughness of the composite material appeared to have increased at the nanoscale after the incorporation of ZIF-72 nanoparticles, thereby increasing the effective contact area during triboelectric charge transfer. Taken together, we conclude that such nanomechanical effects observed from nano-resolved investigations combined to result in the excellent triboelectrification property of ZIF-72/PDMS composites.

### 3.6. Further prototypes of Z72-TENG devices

Example real-world applications of prepared Z72-TENG devices were designed and tested outside a laboratory setting. To improve the compatibility of TENG in practical scenarios, the triboelectric material
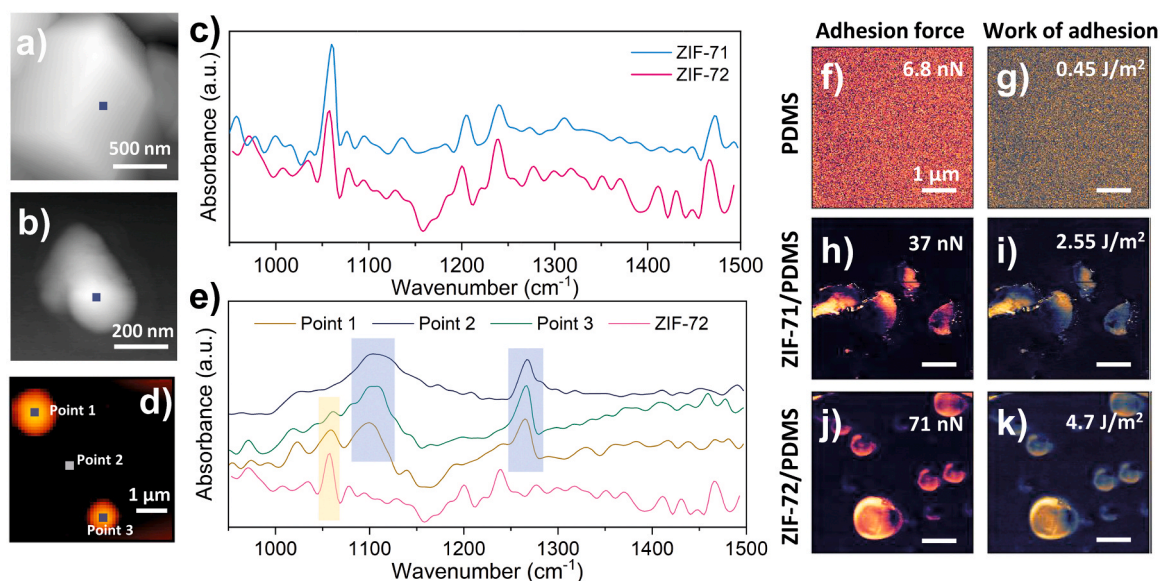
**Fig. 4.** AFM height topography of ZIF-71 single crystal (a), ZIF-72 single crystal (b), and corresponding nano-FTIR absorption spectra (c) measured on positions indicated in (a, b). (d) AFM height topography of the top surface of the ZIF-72/PDMS film. (e) Nano-FTIR absorption spectra measured at points 1–3 as marked in (d). Local distribution of adhesion forces and work of adhesion of PDMS (f,g), ZIF-71/PDMS (h,i), and ZIF-72/PDMS (j,k), highest measured values are indicated on the top-right corners.

was attached onto a flexible substrate instead of a hard 3D-printed board. In addition, by removing the top electrode of the contact-separation mode TENG, a single electrode mode Z72-TENG was fabricated for more versatile applications [52]. Fig. 5a illustrates the operation of TENG from daily human motions, such as touching, tapping, and smashing. The latex glove on the hand acted as a tribo-positive material, thereby transferring charges to the bottom electrode when it is in contact with the prepared ZIF-72/PDMS film. As the tested biomechanical motions were under different contact forces, different voltages were generated in proportion to force with a sensitive response. This demonstration proves the potential application of Z72-TENG to monitor different body motions as well as to harvest energy to enable the powering of portable electronics.

In addition to its application as an energy harvester, the Z72-TENG was also established to be an effective sensor to monitor the surrounding mechanical motions. Here, a prototype for a small TENG-based pedometer was designed to transmit output signal remotely via Bluetooth, as shown in Fig. 5b. The prototype constitutes of a ZIF-based TENG device, a capacitor, a Bluetooth module, and a central Arduino controller. During operation, a mechanical motion to the TENG device triggered a small electrical signal to charge the capacitor, where this small change in the voltage of capacitor was captured and processed by the central controller to generate a pulse signal. With a Bluetooth module integrated to the controller and connected to a mobile software, the stimuli signal was recorded and displayed on a remote device. As Video S3 shows, the operation of the pedometer by tapping the TENG device shows good sensitivity towards the frequency and the force of mechanical motion, demonstrating its excellent potential for self-powered sensors.

Finally, a Morse code generator was developed by leveraging the Z72-TENG. By matching the contact and separation motions of TENG device with "dots" and "dashes" signals in Morse coding, the electrical signal output can be used to represent different letters. Fig. 5c shows the original Morse signal created by Z72-TENG for short messages, with the output message decoded by the Python program. Our result confirms that the Morse code generated is easily recognizable by the computer program. The encoding and decoding of Morse code is also simple and timely to operate, showing an excellent potential of being used as a self-powered transmitter for sending emergency messages at remote places

without any access to a power source. The operating principle of this application is explained further in Note S1.

## 4. Conclusions

In summary, this work demonstrated the effective incorporation of topologically modulated ZIF fillers into PDMS polymer matrix to fabricate mechanically durable TENG devices with outstanding power density. Owing to the high surface charge density, improved dielectric constant and surface adhesion of ZIF-72, the charge generating and charge trapping properties of its nanocomposites are both remarkably improved. We showed for the first time a systematic comparison between the TENG output of a porous versus non-porous MOF constructed from the same chemical building blocks, but with distinctively different framework architecture. Importantly, the triboelectrification mechanisms in ZIF/polymer composites are further investigated through various nanoscale analytical techniques, namely nano-FTIR and TFM, which have not been previously attempted. Among all fabricated MOF-TENG devices, an optimum mass loading of 1 wt % ZIF-72 in PDMS was found to generate the highest electrical output of 578 V and 19 μA, much higher than the pristine PDMS film. An instantaneous power density of ~5 W m$^{-2}$ was also achieved under an external load of 20 MΩ. To illustrate the potential practical applications of the Z72-TENGs, capacitors with different capacitances, LED arrays, and commercial electronics were successfully powered. Lastly, a prototype for a Bluetooth-integrated pedometer and a Morse code generator were constructed which demonstrated a great potential for other innovative real-world applications.

## CRediT authorship contribution statement

**Jiahao Ye:** Conceptualization, Methodology, Formal analysis, Investigation, Writing – Original draft preparation, Writing – review & editing. **Jin-Chong Tan:** Conceptualization, Supervision, Funding acquisition, Writing – review & editing.

## Declaration of Competing Interest

The authors declare the following financial interests/personal
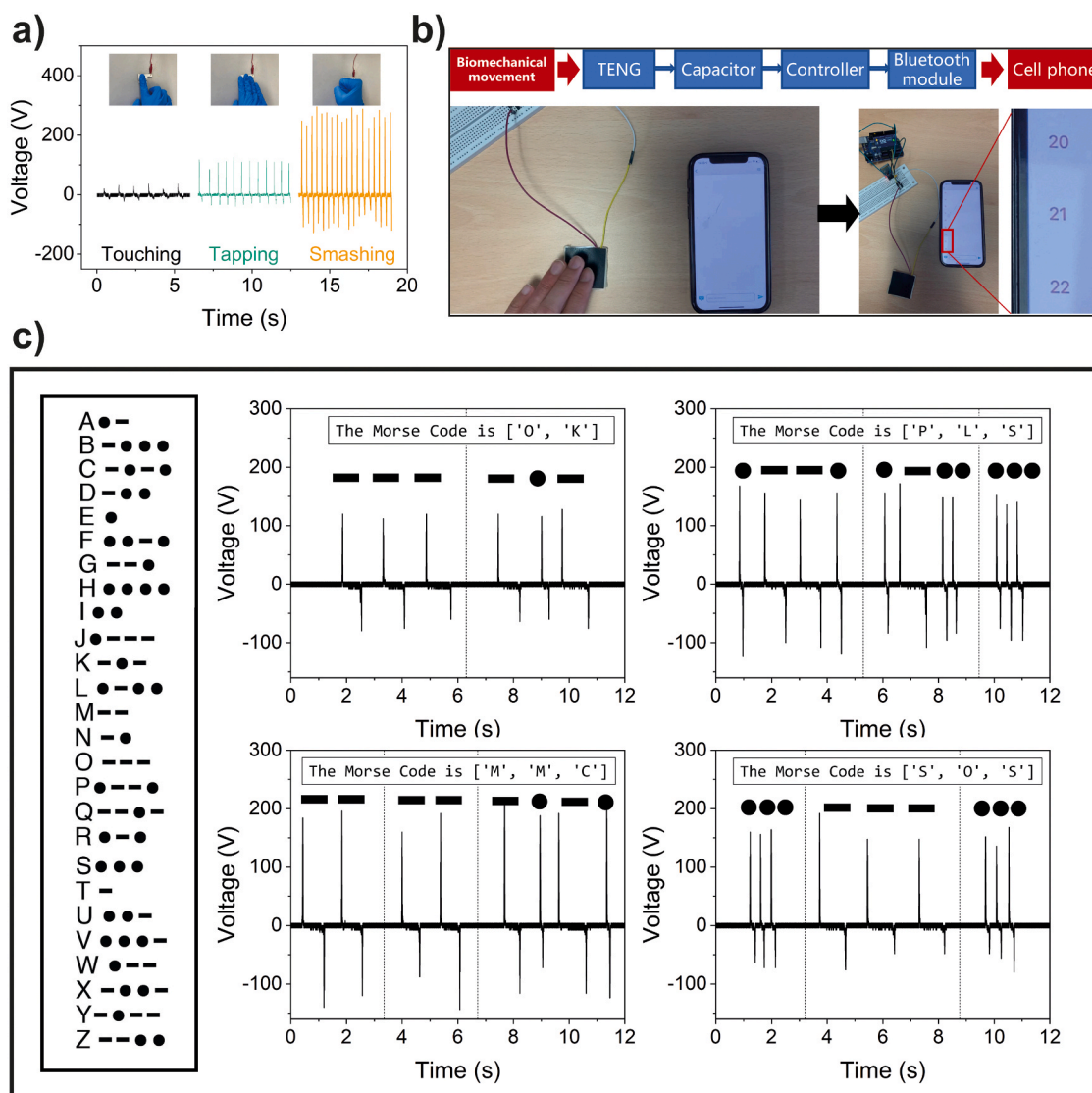
**Fig. 5.** (a) Harvesting biomechanical energy by touching, tapping, and smashing a single-electrode mode Z72-TENG. (b) Schematic of a Z72-TENG based pedometer with Bluetooth transmission; number of taps being detected remotely and displayed on the screen of a mobile phone. (c) International Morse code table for the alphabet (left panel) and the electrical signal output of a 2.25 cm$^2$ Z72-TENG device encoding short messages by hand tapping, translated by a Python program using the coding database. The long signal, represented by a "dash," corresponds to a prolonged contact, while the short signal, denoted as a "dot," is expressed a brief and rapid contact. A video recording is given as Video S4; further details can be found in Note S1 within SI.

relationships which may be considered as potential competing interests: J.Y. and J.C.T. are inventors on UK Patent application no. 2219095.3, which covers zeolitic metal-organic framework based nanocomposites for engineering high-performance triboelectric energy harvesters.

**Data Availability**

Data will be made available on request.

**Acknowledgements**

**Appendix A. Supporting information**

Supplementary data associated with this article can be found in the online version at doi:10.1016/j.nanoen.2023.108687.

**References**

[1] F.-R. Fan, Z.-Q. Tian, Z. Lin Wang, Flexible triboelectric generator, Nano Energy 1 (2012) 328–334, https://doi.org/10.1016/j.nanoen.2012.01.004.

[2] Z. Li, Q. Zheng, Z.L. Wang, Z. Li, Nanogenerator-based self-powered sensors for wearable and implantable electronics, Research (Wash D C) 2020 (2020), 8710686, https://doi.org/10.34133/2020/8710686.

[3] Y. Su, J. Wang, B. Wang, T. Yang, B. Yang, G. Xie, Y. Zhou, S. Zhang, H. Tai, Z. Cai, G. Chen, Y. Jiang, L.Q. Chen, J. Chen, Alveolus-inspired active membrane sensors for self-powered wearable chemical sensing and breath analysis, ACS Nano 14 (2020) 6067–6075, https://doi.org/10.1021/acsnano.0c01804.

[4] D. Wang, D. Zhang, Y. Yang, Q. Mi, J. Zhang, L. Yu, Multifunctional latex/polytetrafluoroethylene-based triboelectric nanogenerator for self-powered organ-

like MXene/metal-organic framework-derived CuO nanohybrid ammonia sensor, ACS Nano 15 (2021) 2911–2919, https://doi.org/10.1021/acsnano.0c09015.

[5] S. Mishra, S. Potu, R.S. Puppala, R.K. Rajaboina, P. Kodali, H. Divi, A novel ZnS nanosheets-based triboelectric nanogenerator and its applications in sensing, self-powered electronics, and digital systems, Mater. Today Commun. 31 (2022), 103292, https://doi.org/10.1016/j.mtcomm.2022.103292.

[6] L. Long, W. Liu, Z. Wang, W. He, G. Li, Q. Tang, H. Guo, X. Pu, Y. Liu, C. Hu, High performance floating self-excited sliding triboelectric nanogenerator for micro mechanical energy harvesting, Nat. Commun. 12 (2021) 4689, https://doi.org/10.1038/s41467-021-25047-y.

[7] R. Walden, C. Kumar, D.M. Mulvihill, S.C. Pillai, Opportunities and challenges in triboelectric nanogenerator (TENG) based sustainable energy generation technologies: a mini-review, Chem. Eng. J. Adv. 9 (2022), 100237, https://doi.org/10.1016/j.ceja.2021.100237.

[8] T. Jin, Z. Sun, L. Li, Q. Zhang, M. Zhu, Z. Zhang, G. Yuan, T. Chen, Y. Tian, X. Hou, C. Lee, Triboelectric nanogenerator sensors for soft robotics aiming at digital twin applications, Nat. Commun. 11 (2020) 5381, https://doi.org/10.1038/s41467-020-19059-3.

[9] C.F. Hu, F. Wang, X.H. Cui, Y.T. Zhu, Recent progress in textile-based triboelectric force sensors for wearable electronics, Adv. Compos. HYBRID Mater. 6 (2023) 70, https://doi.org/10.1007/s42114-023-00650-3.

[10] K. Dong, X. Peng, Z.L. Wang, Fiber/fabric-based piezoelectric and triboelectric nanogenerators for flexible/stretchable and wearable electronics and artificial intelligence, Adv. Mater. 32 (2020), 1902549, https://doi.org/10.1002/adma.201902549.

[11] S. Pan, Z. Zhang, Fundamental theories and basic principles of triboelectric effect: a review, Friction 7 (2019) 2–17, https://doi.org/10.1007/s40544-018-0217-7.

[12] S. Pan, Z. Zhang, Triboelectric effect: a new perspective on electron transfer process, J. Appl. Phys. 122 (2017), 144302, https://doi.org/10.1063/1.5006634.

[13] D.J. Lacks, R.Mohan Sankaran, Contact electrification of insulating materials, J. Phys. D. - Appl. Phys. 44 (2011), 453001, https://doi.org/10.1088/0022-3727/44/45/453001.

[14] J. Chen, Z.L. Wang, Reviving vibration energy harvesting and self-powered sensing by a triboelectric nanogenerator, Joule 1 (2017) 480–521, https://doi.org/10.1016/j.joule.2017.09.004.

[15] R. Zhang, H. Olin, Material choices for triboelectric nanogenerators: a critical review, EcoMat 2 (2020) 12062, https://doi.org/10.1002/eom2.12062.

[16] Y.S. Choi, S.W. Kim, S. Kar-Narayan, Materials-related strategies for highly efficient triboelectric energy generators, Adv. Energy Mater. 11 (2021), 2003802, https://doi.org/10.1002/aenm.202003802.

[17] K. Shrestha, S. Sharma, G.B. Pradhan, T. Bhatta, P. Maharjan, S.S. Rana, S. Lee, S. Seonu, Y. Shin, J.Y. Park, A siloxene/ecoflex nanocomposite-based triboelectric nanogenerator with enhanced charge retention by MoS2/LIG for self-powered touchless sensor applications, Adv. Funct. Mater. 32 (2022), 2113005, https://doi.org/10.1002/adfm.202113005.

[18] J. Chen, H. Guo, X. He, G. Liu, Y. Xi, H. Shi, C. Hu, Enhancing performance of triboelectric nanogenerator by filling high dielectric nanoparticles into sponge PDMS film, ACS Appl. Mater. Interfaces 8 (2016) 736–744, https://doi.org/10.1021/acsami.5b09907.

[19] M. Sahu, S. Hajra, J. Bijelic, D. Oh, I. Djerdj, H.J. Kim, Triple perovskite-based triboelectric nanogenerator: a facile method of energy harvesting and self-powered information generator, Mater. Today Energy 20 (2021) 100639, https://doi.org/10.1016/j.mtener.2021.100639.

[20] M. Salauddin, S.M.S. Rana, M. Sharifuzzaman, M.T. Rahman, C. Park, H. Cho, P. Maharjan, T. Bhatta, J.Y. Park, A novel MXene/Ecoflex nanocomposite-coated fabric as a highly negative and stable friction layer for high-output triboelectric nanogenerators, Adv. Energy Mater. 11 (2021), 2002832, https://doi.org/10.1002/aenm.202002832.

[21] B.N. Chandrashekar, B. Deng, A.S. Smitha, Y. Chen, C. Tan, H. Zhang, H. Peng, Z. Liu, Roll-to-roll green transfer of CVD graphene onto plastic for a transparent and flexible triboelectric nanogenerator, Adv. Mater. 27 (2015) 5210–5216, https://doi.org/10.1002/adma.201502560.

[22] M. Su, B. Kim, Silk fibroin-carbon nanotube composites based fiber substrated wearable triboelectric nanogenerator, ACS Appl. Nano Mater. 3 (2020) 9759–9770, https://doi.org/10.1021/acsanm.0c01854.

[23] I. Stassen, N.C. Burtch, A.A. Talin, P. Falcaro, M.D. Allendorf, R. Ameloot, An updated roadmap for the integration of metal-organic frameworks with electronic devices and chemical sensors, Chem. Soc. Rev. 46 (2017) 3185–3241, https://doi.org/10.1039/c7cs00122c.

[24] M. Gutiérrez, Y. Zhang, J.-C. Tan, Confinement of luminescent guests in metal–organic frameworks: understanding pathways from synthesis and multimodal characterization to potential applications of LG@MOF systems, Chem. Rev. 122 (2022) 10438–10483, https://doi.org/10.1021/acs.chemrev.1c00980.

[25] J. Lee, O.K. Farha, J. Roberts, K.A. Scheidt, S.T. Nguyen, J.T. Hupp, Metal-organic framework materials as catalysts, Chem. Soc. Rev. 38 (2009) 1450–1459, https://doi.org/10.1039/b807080f.

[26] J.R. Li, R.J. Kuppler, H.C. Zhou, Selective gas adsorption and separation in metal-organic frameworks, Chem. Soc. Rev. 38 (2009) 1477–1504, https://doi.org/10.1039/b802426j.

[27] A.S. Babal, L. Donà, M.R. Ryder, K. Titov, A.K. Chaudhari, Z. Zeng, C.S. Kelley, M. D. Frogley, G. Cinque, B. Civalleri, J.-C. Tan, Impact of pressure and temperature on the broadband dielectric response of the HKUST-1 metal–organic framework, J. Phys. Chem. C. 123 (2019) 29427–29435, https://doi.org/10.1021/acs.jpcc.9b08125.

[28] K. Titov, Z. Zeng, M.R. Ryder, A.K. Chaudhari, B. Civalleri, C.S. Kelley, M. D. Frogley, G. Cinque, J.-C. Tan, Probing dielectric properties of metal–organic

frameworks: MIL-53(Al) as a model system for theoretical predictions and experimental measurements via synchrotron far- and mid-infrared spectroscopy, J. Phys. Chem. Lett. 8 (2017) 5035–5040, https://doi.org/10.1021/acs.jpclett.7b02003.

[29] R. Wen, J. Guo, A. Yu, J. Zhai, Z. l Wang, Humidity-resistive triboelectric nanogenerator fabricated using metal organic framework composite, Adv. Funct. Mater. 29 (2019), 1807655, https://doi.org/10.1002/adfm.201807655.

[30] N. Jayababu, D. Kim, Co/Zn bimetal organic framework elliptical nanosheets on flexible conductive fabric for energy harvesting and environmental monitoring via triboelectricity, Nano Energy 89 (2021), 106355, https://doi.org/10.1016/j.nanoen.2021.106355.

[31] S.M.S. Rana, M.A. Zahed, M.T. Rahman, M. Salauddin, S.H. Lee, C. Park, P. Maharjan, T. Bhatta, K. Shrestha, J.Y. Park, Cobalt-nanoporous carbon functionalized nanocomposite-based triboelectric nanogenerator for contactless and sustainable self-powered sensor systems, Adv. Funct. Mater. 31 (2021), 2105110, https://doi.org/10.1002/adfm.202105110.

[32] R. Wen, L. Fan, Q. Li, J. Zhai, A composite triboelectric nanogenerator based on flexible and transparent film impregnated with ZIF-8 nanocrystals, Nanotechnology 32 (2021), 345401, https://doi.org/10.1088/1361-6528/ac020f.

[33] Y. Zhang, M. Gutiérrez, A.K. Chaudhari, J.-C. Tan, Dye-encapsulated zeolitic imidazolate framework (ZIF-71) for fluorochromic sensing of pressure, temperature, and volatile solvents, ACS Appl. Mater. Interfaces 12 (2020) 37477–37488, https://doi.org/10.1021/acsami.0c10257.

[34] M. Tu, D.E. Kravchenko, B. Xia, V. Rubio-Gimenez, N. Wauteraerts, R. Verbeke, I.F. J. Vankelecom, T. Stassin, W. Egger, M. Dickmann, H. Amenitsch, R. Ameloot, Template-mediated control over polymorphism in the vapor-assisted formation of zeolitic imidazolate framework powders and films, Angew. Chem. Int. Ed. 60 (2021) 7553–7558, https://doi.org/10.1002/anie.202014791.

[35] A.F. Möslein, M. Gutiérrez, B. Cohen, J.-C. Tan, Near-field infrared nanospectroscopy reveals guest confinement in metal–organic framework single crystals, Nano Lett. 20 (2020) 7446–7454, https://doi.org/10.1021/acs.nanolett.0c02839.

[36] S. Niu, S. Wang, L. Lin, Y. Liu, Y.S. Zhou, Y. Hu, Z.L. Wang, Theoretical study of contact-mode triboelectric nanogenerators as an effective power source, Energy Environ. Sci. 6 (2013) 3576–3583, https://doi.org/10.1039/C3EE42571A.

[37] B. Yang, W. Zeng, Z.H. Peng, S.R. Liu, K. Chen, X.M. Tao, A fully verified theoretical analysis of contact-mode triboelectric nanogenerators as a wearable power source, Adv. Energy Mater. 6 (2016), 1600505, https://doi.org/10.1002/aenm.201600505.

[38] Z. Chen, Y. Cao, W. Yang, L. An, H. Fan, Y. Guo, Embedding in-plane aligned MOF nanoflakes in silk fibroin for highly enhanced output performance of triboelectric nanogenerators, J. Mater. Chem. A 10 (2022) 799–807, https://doi.org/10.1039/d1ta08605g.

[39] Q. Chen, Y. Shen, S. Zhang, Q.M. Zhang, Polymer-based dielectrics with high energy storage density, Annu. Rev. Mater. Res. 45 (2015) 433–458, https://doi.org/10.1146/annurev-matsci-070214-021017.

[40] M.R. Ryder, Z. Zeng, K. Titov, Y. Sun, E.M. Mahdi, I. Flyagina, T.D. Bennett, B. Civalleri, C.S. Kelley, M.D. Frogley, G. Cinque, J.-C. Tan, Dielectric properties of zeolitic imidazolate frameworks in the broad-band infrared regime, J. Phys. Chem. Lett. 9 (2018) 2678–2684, https://doi.org/10.1021/acs.jpclett.8b00799.

[41] W.J. Li, J. Liu, Z.H. Sun, T.F. Liu, J. Lu, S.Y. Gao, C. He, R. Cao, J.H. Luo, Integration of metal-organic frameworks into an electrochemical dielectric thin film for electronic applications, Nat. Commun. 7 (2016) 11830, https://doi.org/10.1038/ncomms11830.

[42] J.E. Huheey, The electronegativity of groups, J. Phys. Chem. 69 (1965) 3284–3291, https://doi.org/10.1021/j100894a011.

[43] J.H. Lee, I. Yu, S. Hyun, J.K. Kim, U. Jeong, Remarkable increase in triboelectrification by enhancing the conformable contact and adhesion energy with a film-covered pillar structure, Nano Energy 34 (2017) 233–241, https://doi.org/10.1016/j.nanoen.2017.02.032.

[44] M.T. Rahman, S.M.S. Rana, M.A. Zahed, S. Lee, E.-S. Yoon, J.Y. Park, Metal-organic framework-derived nanoporous carbon incorporated nanofibers for high-performance triboelectric nanogenerators and self-powered sensors, Nano Energy 94 (2022), 106921, https://doi.org/10.1016/j.nanoen.2022.106921.

[45] T. Vijayakanth, A.K. Srivastava, F. Ram, P. Kulkarni, K. Shanmuganathan, B. Praveenkumar, R. Boomishankar, A flexible composite mechanical energy harvester from a ferroelectric organoamino phosphonium salt, Angew. Chem. Int. Ed. 57 (2018) 9054–9058, https://doi.org/10.1002/anie.201805479.

[46] Y. Guo, Y. Cao, Z. Chen, R. Li, W. Gong, W. Yang, Q. Zhang, H. Wang, Fluorinated metal-organic framework as bifunctional filler toward highly improving output performance of triboelectric nanogenerators, Nano Energy 70 (2020), 104517, https://doi.org/10.1016/j.nanoen.2020.104517.

[47] Y.M. Wang, X. Zhang, D. Yang, L. Wu, J. Zhang, T. Lei, R. Yang, Highly stable metal-organic framework UiO-66-NH2 for high-performance triboelectric nanogenerators, Nanotechnology 33 (2021), 065402, https://doi.org/10.1088/1361-6528/ac32f8.

[48] R. Wen, B. Zhao, L. Fan, J. Guo, J. Zhai, Controlling the output performance of triboelectric nanogenerator through filling isostructural metal–organic frameworks with varying functional groups, Adv. Mater. Technol. 8 (2023), 2201330, https://doi.org/10.1002/admt.202201330.

[49] A.F. Möslein, J.-C. Tan, Vibrational modes and terahertz phenomena of the large-cage zeolitic imidazolate framework-71, J. Phys. Chem. Lett. 13 (2022) 2838–2844, https://doi.org/10.1021/acs.jpclett.2c00081.

[50] L. Lapčinskis, K. Mālnieks, J. Blūms, M. Knite, S. Oras, T. Käämbre, S. Vlassov, M. Antsov, M. Timusk, A. Šutka, The adhesion-enhanced contact electrification and

efficiency of triboelectric nanogenerators, Macromol. Mater. Eng. 305 (2020), 1900638, https://doi.org/10.1002/mame.201900638.

[51] W. Yang, X. Wang, P. Chen, Y. Hu, L. Li, Z. Sun, On the controlled adhesive contact and electrical performance of vertical contact-separation mode triboelectric nanogenerators with micro-grooved surfaces, Nano Energy 85 (2021), 106037, https://doi.org/10.1016/j.nanoen.2021.106037.

[52] A. Manjari Padhan, S. Hajra, M. Sahu, S. Nayak, H. Joon Kim, P. Alagarsamy, Single-electrode mode TENG using ferromagnetic NiO-Ti based nanocomposite for effective energy harvesting, Mater. Lett. 312 (2022), 131644, https://doi.org/10.1016/j.matlet.2021.131644.

**Jin-Chong Tan** is Professor of Nanoscale Engineering in the Department of Engineering Science at Oxford University. He received his BEng (UTM Malaysia, 1999) and MEng (NTU Singapore, 2001) in mechanical & materials engineering, and Ph.D. in materials science (2005) from Cambridge University. In 2012, he founded the MMC Lab at Oxford, focusing on the physical and functional properties of novel materials targeting real-world applications. Recent research interests include nanoengineering of composites for energy, structural, and sensing technologies.

**Jiahao Ye** received his MEng degree in Chemical Engineering from Imperial College London in 2021. He is currently a DPhil student in the Department of Engineering Science at Oxford University. His current research focuses on metal-organic frameworks, polymers, nanocomposites, triboelectric nano-generators, self-powered sensors, and energy harvesting devices.